Chinese Journal of Aeronautics, (2022), 35(10): 118–133

Chinese Society of Aeronautics and Astronautics
& Beihang University

Chinese Journal of Aeronautics

cja@buaa.edu.cn
www.sciencedirect.com

Experimental study of hysteresis and catastrophe in a cavity-based scramjet combustor

Xu ZHANG [a,b], Qifan ZHANG [a,*], Zhenjie WU [a,b], Lianjie YUE [a,b], Zhanbiao GAO [a], Weihang LUO [a], Hao CHEN [a,c]

[a] *State Key Laboratory of High Temperature Gas Dynamics, Institute of Mechanics, Chinese Academy of Sciences, Beijing 100190, China*
[b] *School of Engineering Science, University of Chinese Academy of Sciences, Beijing 100049, China*
[c] *Innovation Academy for Light-duty Gas Turbine, Chinese Academy of Sciences, Beijing 100190, China*

Received 6 May 2021; revised 27 June 2021; accepted 13 July 2021
Available online 16 September 2021

KEYWORDS

Catastrophe;
Cavity-based scramjet;
Flame stabilization;
Flame/shock interaction;
Hysteresis

Abstract Hystereses and catastrophes were experimentally investigated in a cavity-based scramjet combustor. The inflow Mach number was 3.0. Fuel Equivalence Ratio (ER) was continuously regulated with multi-steps to explore influences of historical regulation directions on combustion states. Two divided hysteresis loops with catastrophes were observed. By 1-D flow estimations, the first loop occurred with shock-free/separated scramjet mode transitions, while the second kept in the separated scramjet mode. This breaks through the traditional knowledge that hysteresis and catastrophe were certainly related to ramjet/scramjet mode transitions. The first hysteresis and catastrophes were attributed to flame stabilization mode transitions between the cavity shear-layer stabilized and the jet-wake stabilized, with flow separation establishment/vanishment upstream the cavities. The obvious variations of flame and shock/separation structures meant large wall-pressure changes in the expansive duct, and generated obvious thrust catastrophes. Besides, transition ER and catastrophe were larger in historical ER-increasing path because combustion efficiency became obviously larger as flow separation established. Difference of critical transition ERs meant the first hysteresis. The second hysteresis and catastrophes in the jet-wake stabilized mode were attributed to flame/shock interaction mode transitions between the flame/shock weak interaction mode and intensive interaction mode. Each transition caused slightly stronger/weaker flame interacting with slightly larger/smaller flow separation, which meant small wall-pressure changes

* Corresponding author.
E-mail address: zhangqifan@imech.ac.cn (Q. ZHANG).
Peer review under responsibility of Editorial Committee of CJA.

Production and hosting by Elsevier

https://doi.org/10.1016/j.cja.2021.08.008

Nomenclature

F	measured thrust
F_{ta}	thrust augmentation
Ma	Mach number
p	pressure
T	temperature
Δt_t	a time interval of many transient CH* chemiluminescence images
Δt_c	a time interval close to camera recording period
x	x coordinate in a Cartesian coordinate system

Sub/Supscript

CC	current case
cv	cavity bottom wall-pressure tap
H	the higher value
in	test-section inlet
L	the lower value
min	the minimum value
NF	case under current inflow but with no fuel injection
ref	reference value
*	stagnation state
-	time-averaged value

in the expansive duct, and thus thrust catastrophe was unobvious. Hysteresis occurred as the critical transition ER was slightly higher in historical ER-increasing path because of slightly lower combustion efficiency under slightly smaller separation.

1. Introduction

Scramjet engines provide propulsions for hypersonic air-breathing flights.[1] A scramjet combustor generally contains a constant-area isolator and an expansive duct. Former researchers[2–5] observed hysteresis in scramjet combustors, showing as two possible wall-pressure distributions at a certain fuel Equivalence Ratio (ER) condition depending on historical ER regulation directions (decreasing or increasing). Combustion hysteresis is a mathematically[6] dual-solution phenomenon, indicating two possible types of combustion states at a certain ER. The two transitions between the two states would probably cause abrupt changes named as catastrophes, which were observed in previous studies.[7–12] If the two critical ERs of transitions from each state were different, then a hysteresis loop would appear.[13] In other words, hysteresis is intrinsically related to the catastrophes across the two transitions. Hysteresis and catastrophe in scramjet combustors were likely to generate hysteresis and catastrophe of wall-pressures and thrusts, which were adverse for flight controls. Consequently, in-depth knowledge of hysteresis and catastrophe mechanisms is important and essential for flight control designs.

To analyze experimental wall-pressure data of a scramjet combustor, a quick method is to solve 1-D flow equations,[1,14–19] and 1-D Mach number distribution can be obtained at a certain ER condition. A scramjet combustor is traditionally divided into two types of combustion states, namely the ramjet (subsonic combustion) mode and the scramjet (supersonic combustion) mode, respectively.[1] They can be distinguished by the minimum Mach number Ma_{min} of 1-D flow distribution. If $Ma_{min} < 1$, then it is the ramjet mode, as the flow is thermally choked somewhere, otherwise it is the scramjet mode. The scramjet mode is subdivided into the separated scramjet mode and the shock-free scramjet mode. "Separated" means shock-train and flow separation occurred upstream because of enough backpressure-rise by heat release, and "shock-free" means not.

As combustor inflows are supersonic and easy to cause flameout, flameholders such as ramps,[2] gas-portfires [3,20,21], struts[4,5,22,23] and cavities[5,24,25] are commonly installed in scramjet combustors. Hystereses were observed based on different flameholders.[2–5,26] Rockwell et al. [2] first observed hysteresis in a ramp-based combustor under clean-air inflow condition. They argued hysteresis occurred with ramjet/scramjet mode transitions, and proved catastrophe and hysteresis of thrusts by wall-pressure integrations. The importance of historical ER regulation directions on wall-pressure distributions was likewise demonstrated by Wei et al. [3] in a gas-portfire-based combustor. Bao et al. [4] observed hysteresis in a strut-based combustor, occurring with transitions between the ramjet modes with one and two thermal choking points, respectively. In a strut-cavity-based combustor, Zhu and Xu[5] observed hysteresis with transitions between the supersonic combustion mode and the subsonic combustion mode. They claimed that differences of heat releases under different combustion modes brought about the hysteresis. Yang et al.[27] analytically thought the ramjet-scramjet mode transition was closely related to the thermal choking effects and shock wave motion. Feng et al.[26] further numerically explicated the interaction between the oblique shock train motion and combustion heat release contributed to hysteresis in a variable geometry combustor.

Thrust catastrophe is a phenomenon bad for flight control, and thus was concerned by previous studies.[7–12,28] Sullins[28] first measured thrust during the transition from the ramjet mode to the shock-free scramjet mode in a backward-step-based combustor, but no thrust catastrophe was observed. In a strut-based combustor, Chang et al.[7] observed an abrupt increase of thrust when combustion transited from the sepa-

rated scramjet mode to the ramjet mode. Xiao et al.[8] studied a cavity-backward-step-based combustor. They observed abrupt increase and decrease of thrusts during the two transitions between the shock-free scramjet mode and the ramjet mode, respectively. Mitani et al.[9] defined the intensive combustion mode and the weak combustion mode by higher and lower thrust performances, respectively. Then, Ueda et al.[10] observed an abrupt increase of thrust from the weak combustion mode to the intensive combustion mode in a strut-based engine. Kouchi et al.[11] numerically claimed driving force of the transition was combustion-generated high pressure, which caused upstream propagation of the combustion region with boundary-layer separation. Turner and Smart [12] observed transitions from the shock-free scramjet mode to the separated scramjet mode in two slightly different combustors both without flameholders, but thrust catastrophe only occurred in one combustor.

Thrusts originate from integrations of wall pressures and frictions. But phenomenally, above studies[2–5,7,8,12] commonly measured wall-pressures without thrusts, lacking direct data to concurrently testify hysteresis and catastrophe of both wall-pressures and thrusts. Besides, previous studies utilized wall-pressures at a few positions to estimate thrusts, which were not convictive enough to recognize catastrophes. Mechanically, above studies commonly explained hysteresis and catastrophe with the ramjet/scramjet modes by 1-D flow estimations of thermal chokings, or even with the intensive/weak combustion modes which were not strictly defined. But 1-D estimations had inherent large errors, and only based on experimental wall-pressure data, lacking more convincing data supports. Intrinsically, scramjet combustors involve strongly nonlinear structures such as flames, shocks and separations, which are the foundations of hysteresis and catastrophe, and could not be described in 1-D flow estimations. Wall-normal fuel injections upstream cavity flameholders are popular designs in combustors[8,14,18,19,24,25] for low pressure losses and cooling requirements. Former studies employed flameholders generating strong shocks, and were more likely to generate hysteresis and catastrophe. But the popular cavity flameholders do not generate strong shock. Hysteresis and catastrophe in cavity-based combustors had not been experimentally studied yet.

As techniques developed, researchers could obtain instantaneous images of 2-D flame distributions by high-speed photography of combustion luminosity or chemiluminescence.[29–40] For the generally used ethylene/kerosene fuel, compared to wideband combustion luminosity, narrow-band CH* chemiluminescence is a more reasonable marker of heat release intensity.[30] Thus, high-speed photographs of CH* chemiluminescence were more prevalent in recent studies.[29–36] Using these optical methods, researchers could directly observe flame structures in scramjet combustors. For a cavity-based combustor, Micka and Driscoll[29] first depicted two kinds of combustion states by 2-D flame distributions. The two states are called the jet-wake stabilized mode and the cavity stabilized mode, which had different stabilized locations of flame front. The flame front was upstream the cavity in the jet-wake stabilized mode, and might be ahead of or behind the fuel injectors. In contrast, the flame front was downstream the cavity fore-wall in the cavity stabilized mode. This mode was subdivided into the combined cavity shear-layer/recirculation stabilized mode and the cavity shear-layer stabilized mode by Sun et al.[37]. The difference was that the combined mode had distinct flame in the cavity recirculation region, but the cavity shear-layer stabilized mode did not. Previous studies provided good knowledges of flame stabilization characteristics in cavity-based scramjet combustors. However, the relation between flame stabilizations and hysteresis and catastrophe remained unclear. Unlike former explanations of hysteresis and catastrophe by large-error 1-D flow estimations, in-depth explanation remained to be done from the viewpoint of flame/flow structures. Our previous numerical study[41] preliminarily demonstrated that hysteresis and catastrophe were not necessarily related to the ramjet/scramjet mode transitions, and could be strongly related to transitions between different flame stabilization modes, which guided the current experimental study.

The current study focuses on hysteresis and catastrophe in a cavity-based scramjet combustor. Cavity flamholders were installed in the expansive duct of the combustor. Ethylene fuel was injected wall-normally upstream the cavities. Combustion tests were performed under the inflow corresponding to a Mach number 6.0 flight condition. To consider the influence of historical ER variation directions on combustion states, a multi-step ER regulation method was employed in each test. Multiple measuring methods were implemented to acquire comprehensive data, including wall-pressures, thrusts and high-speed images of shadowgraphs and CH* chemiluminescence. Section 2 introduces the test facility, combustor model, measuring methods and test scheme. Section 3.1 illustrates hysteresis and catastrophe features of two divided hysteresis loops, and their relations with traditional ramjet/scramjet modes by 1-D flow analyses. Then from the viewpoint of practical flow and flame structures, in-depth mechanisms of the two kinds of hystereses and catastrophes are further elucidated in Sections 3.2 and 3.3, respectively.

2. Experimental setup

2.1. Test facility and typical time sequence

Experiments were done using a direct-connect supersonic combustion test facility in the Institute of Mechanics, Chinese Academy of Sciences. Fig. 1 shows a schematic of the facility. Test gases successively passed through a heater, a Laval nozzle, a test-section and a tail-section, and then off-gases were exhausted outside through an exhaust pipe. Certain fluxes of air, hydrogen and oxygen were injected into the heater by pressure regulating valves and critical flow Venturi nozzles. The heater organized sufficient combustion of the injected gases. The products in heater kept 21% oxygen in mole fraction, and had predetermined total pressure and total enthalpy to match a flight condition. The heated gases were accelerated to supersonic by the Laval nozzle, and then served as the inflow for test-section.

Fig. 2 shows typical time sequence of each test. The heater provided test-section inflow for about 4 s from t_0 to t_8. Pilot hydrogen was injected into the test-section from t_1 to t_4, and ignited by the spark ignitor operating during t_0 and t_2. Ethylene fuel was injected into the test-section from t_3 to t_8, and was ignited by the pilot flame immediately. Efficient test time of ethylene combustion was about 2 s between t_5 and t_8, during which no pilot hydrogen existed.

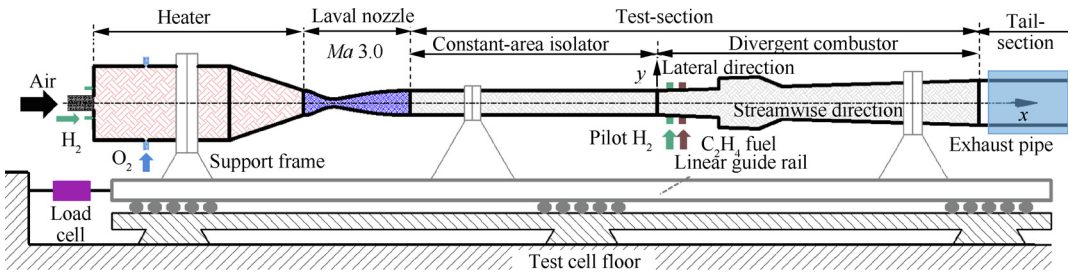

Fig. 1 Schematic of direct-connect test facility.

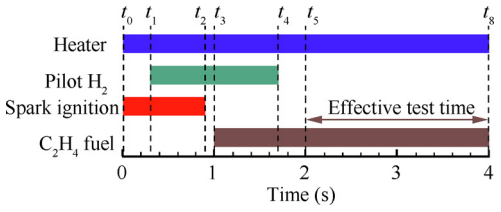

Fig. 2 Typical time sequence of each test.

2.2. Combustor model and measuring methods

Fig. 3 is a 2-D schematic diagram of the laterally symmetric test-section combustor, which included a 400 mm long constant-area isolator and a 520 mm long 3.6° expansive duct. The combustor width was constantly 80 mm, and the inlet was 40 mm high. Cavities and injectors were installed in the expansive duct, and their configurations and sizes are displayed in Fig. 4. The 17 mm-deep 65 mm-long cavity spanned the combustor width in spanwise direction. The cavity's leading edge was located 100 mm downstream the isolator exit, and the trailing edge was 67.5° sweepback. On the combustor's upper/lower wall, six diameter 0.7 mm hydrogen injection holes and nine diameter 1.0 mm ethylene injection holes were configured crossways in spanwise direction, and a spark igniter was installed centrally. They were located 20, 40, 75 mm downstream the isolator exit, respectively. A pressure regulating valve was utilized for continuous flux regulations of ethylene injection. The flux was measured by an orifice plate flowmeter with a 0.4–40 kPa range 0.1% accuracy differential pressure transmitter.

Multiple measuring methods were applied, including measurements of wall-pressures and thrusts, and high-speed photography of shadowgraphs and CH* chemiluminescence. For

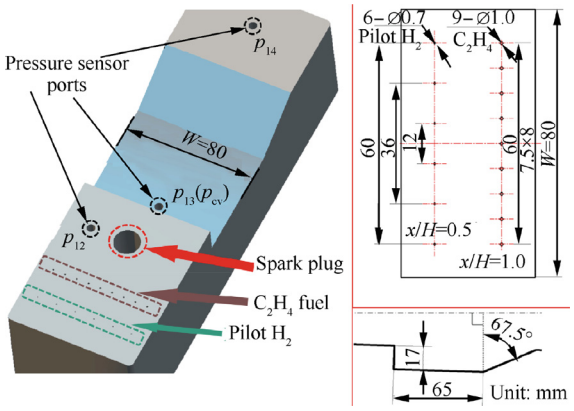

Fig. 4 Cavity and injectors' configuration and sizes.

the purpose of thrust measuring, as shown in the above Fig. 1, the heater, nozzle, test-section and tail-section were fixed coaxially and horizontally on a linear sliding guide rail. A 4448 N range 0.25% accuracy "OMEGA LC203-1 K" load cell was installed on the rail's left-side, and sampled thrusts at 100 Hz by a "Pacific-Instruments series 6000" data acquisition system. To reduce errors, all gas supply pipes employed steel flexible hose, and the tail-section kept contactless from the exhaust pipe. Thrust F_{ta} hereunder meant thrust augmentation as below:

$$F_{ta} = F_{CC} - F_{NE} \tag{1}$$

where F_{CC} and F_{NE} represented the measured thrusts of the case at current ER condition, and the case with no fuel injection, respectively.

As shown in Fig. 3, to measure wall-pressures, there were nineteen diameter 0.8 mm 3 mm-depth taps on the upper and lower walls, respectively. These taps were marked as p_1-

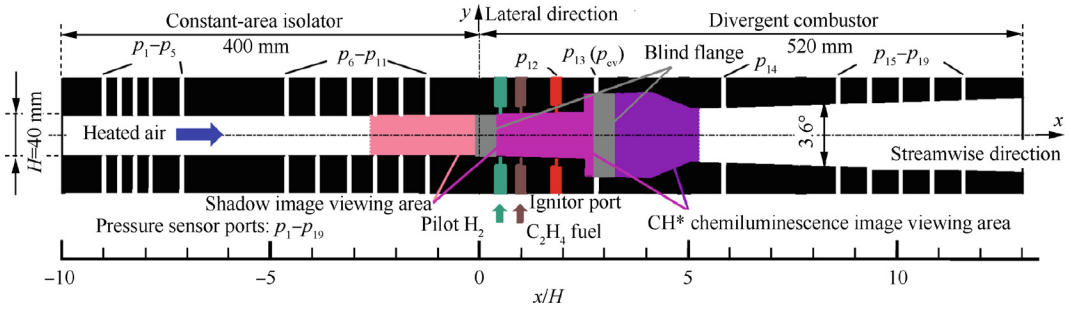

Fig. 3 Schematic diagram of test-section combustor.

p_{19} according to their streamwise positions, and located symmetrically in spanwise direction except p_{12}, which as shown in Fig. 4, was located near the sidewall as the spark ignitor was installed symmetrically. The wall-pressures were measured by 826 kPa range "TE-Connectivity ESP-32HD" electronic-scanned pressure sensors, and sampled by a "DTC Initium" pressure acquisition system at 653 Hz. As wall-pressure data at the same streamwise positions were similar, wall-pressure analyses in Section 3 will not mention the upper and lower walls.

Shadowgraph is commonly used for flow visualization of shocks and flow separations in supersonic flows.[42,43] Luminous intensities of CH* chemiluminescence can provide markers of the heat release rates in ethylene-fueled combustors.[29–33] In this paper, photographies of shadowgraph and CH* chemiluminescence were both utilized, and recorded by two high-speed cameras, respectively. The 2-D observation regions are displayed in Fig. 3 with different colors. Shadowgraph region was around the injectors to observe combustion-induced flow separations and shocks. CH* chemiluminescence region was around the cavities to observe flame stabilizations. The region between the injectors and the cavities was observed by both methods. The shadowgraph used a tungsten lamp light source. The images were recorded by a "FASTCAM Mini UX50" camera at 2000 frame/s, 0.03 ms exposure time and 1280 pixel × 536 pixel spatial resolution. CH* chemiluminescence was observed through a ±10 mm bandwidth optical filter centered at 430 nm. The images were recorded by a "FASTCAM SA4" camera at 4000 frame/s, 0.25 ms exposure time and 896 pixel × 464 pixel spatial resolution.

Besides the above measuring methods, to monitor injection pressures, two pressure transmitters were installed on the hydrogen and ethylene fuel supply pipes, respectively. The two pressures were recorded at 100 Hz by the aforementioned "Pacific-Instruments series 6000" data acquisition system. All experimental data acquisitions were triggered by the same Transistor-Transistor Logic (TTL) signal source to ensure recording time consistency of these data.

2.3. Inflow condition and test scheme

In this paper, the test-section inflow was constant, which simulated a flight condition of Mach number 6.0 and height 27 km. Table 1 lists the detailed inflow parameters. The inflow Mach number, stagnation temperature and stagnation pressure were 3.0, 1657 K and 2100 kPa, respectively. The inflow static pressure was $p_{in} = 40$ kPa, and is used below as the reference pressure p_{ref} for normalizations of wall-pressure data.

This work studied combustion hysteresis, which meant the effects of historical ER variation directions on combustion states. To consider these effects, a multi-step ER regulation method was used in each test, in which ER was regulated step by step to certain target ER condition. Fig. 5 illustrates the regulation method, in which the red and the black lines represent the regulation paths for historical ER decreasing and increasing directions, respectively. Current test scheme referred to former numerical study [41] which claimed that hysteresis could result from transitions between the jet-wake stabilized mode and the cavity shear-layer stabilized mode in cavity-based combustors, which had not be experimentally observed by previous hysteresis studies [2–5,26]. Consequently, at an initial ER condition in Fig. 5, the flame should be in the jet-wake stabilized mode if it was in historical ER decreasing path, and should be in the cavity shear-layer stabilized mode if it was in historical ER increasing path.

Table 1 Test-section inflow parameters.

Parameter	Ma_{in}	T^*_{in}(K)	p^*_{in}(kPa)
Value	3.0	1657	2100

3. Results and discussion

Tests were performed by the scheme in Section 2.3, and two divided hysteresis loops were observed, indicating two different kinds of combustion hystereses. Section 3.1 illustrates basic hysteresis and catastrophe features, and recognizes their relations with ramjet/scramjet mode transitions by traditional 1-D flow analyses.[14] Then by detailed analyses from the viewpoint of practical flame and flow structures, in-depth occurrence mechanisms of hystereses and catastrophes are further elucidated in Section 3.2 and 3.3, respectively.

3.1. Two kinds of combustion hystereses

In a cavity-based combustor, flame commonly exists near cavities, and thus the cavity bottom pressure p_{cv} can represent combustion status. Fig. 6 depicts the time-averaged pressure $\bar{p}_{cv}$ at different target ER conditions. A hollow/solid diamond symbol means $\bar{p}_{cv}$ at each target ER condition, and is normalized by the reference pressure p_{ref} mentioned in Section 2.3. This chart illustrates two divided hysteresis loops, differing from former studies of only one loop [2–5,26], and experimentally verified our former numerical study.[41] The results were experimentally repeated for reliability. The first and the second hysteresis loops occurred between the ER ranges of 0.13–0.42 and 0.52–0.68, respectively. The first loop was much larger than the second. Meanwhile, in both hysteresis ER ranges, $\bar{p}_{cv}$ depended on historical ER variation directions. $\bar{p}_{cv}$ was higher in historical ER-decreasing path than ER-increasing.

Fig. 7 displays time-averaged thrust $\bar{F}_{ta}$ at different target ER conditions. Figs. 6 and 7 show that thrusts and cavity bottom wall-pressures had similar trends as target ER differed. Meanwhile, thrust and wall-pressure synchronously underwent catastrophes across critical target ER conditions. For instance,

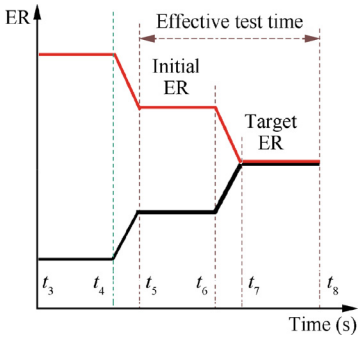

Fig. 5 Sketch of multi-step ER regulations.

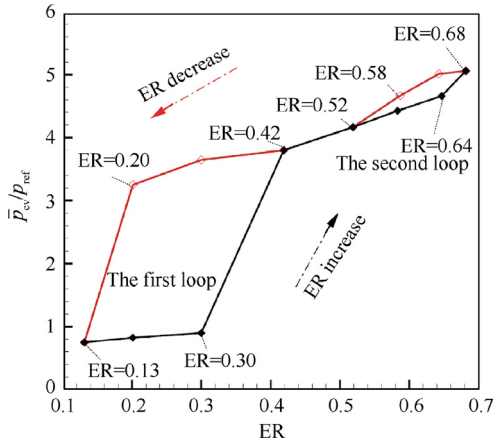

Fig. 6 Normalized cavity bottom pressure $\bar{p}_{cv}/p_{ref}$ vs target ER condition.

thrust and wall-pressure abruptly increased from target ER = 0.30 to ER = 0.42 conditions in historical ER-increasing path. This proved the direct relation between catastrophes of thrust and wall-pressure. Besides, it should be noted in the first loop, thrust catastrophe was much larger in historical ER-increasing path than ER-decreasing.

Quantificationally, catastrophe degree χ_ψ is defined as below:

$$\chi_\psi = \frac{\psi_H - \psi_L}{\psi_H} \cdot 100\% \tag{2}$$

where ψ represents $\bar{p}_{cv}$ or $\bar{F}_{ta}$, and subscripts "H" and "L" denote the higher and lower values of ψ, respectively. Catastrophe degrees of cavity bottom pressure $\chi_{\bar{p}_{cv}}$ and thrust $\chi_{\bar{F}_{ta}}$ at different target ER conditions are listed in Table 2, which illustrates the first hysteresis loop included much larger catastrophes than the second. For example, $\chi_{\bar{p}_{cv}}$ and $\chi_{\bar{F}_{ta}}$ were 70% and 40% at target ER = 0.20 in the first loop, but only 5% and 11% at target ER = 0.58 in the second, respectively. This also indicated the two divided hysteresis loops included two different kinds of hystereses and relevant catastrophes. Besides, Table 2 shows $\chi_{\bar{p}_{cv}}$ and $\chi_{\bar{F}_{ta}}$ differed a little at the same target ERs. The quantificational differences demonstrated

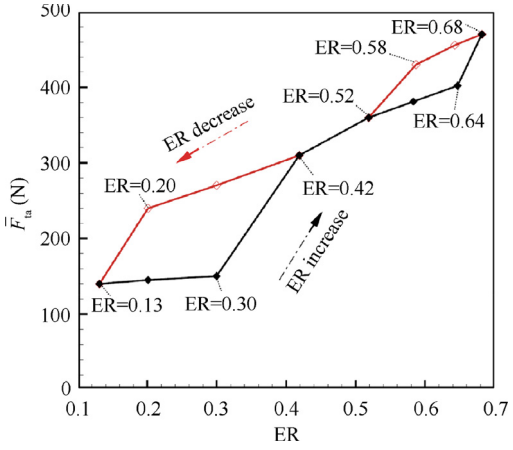

Fig. 7 Time-averaged thrust $\bar{F}_{ta}$ vs target ER condition.

thrust and wall-pressure variations were not absolutely consistent. This is because thrust is mainly composed of wall-pressure integration in the entire expansive duct, and wall-pressure variations along the duct generally did not vary in equal proportion. Thus, a single port wall-pressure variation did not absolutely accord with thrust variation.

To understand hystereses and catastrophes from the traditional angle of 1-D flow thermal choking, wall-pressure data are one-dimensionally analyzed to recognize ramjet/scramjet mode.[14] Fig. 8 shows typical 1-D pressure p/p_{ref} and Mach number Ma distributions at target ER = 0.30 and ER = 0.42 conditions in historical ER-increasing path, respectively. At ER = 0.30, the obviously streamwise low pressures and $Ma_{min} > 1.0$ indicated the shock-free scramjet mode. At ER = 0.42, the streamwise high pressures and the pressure-rise origin ahead of injectors meant flow separation, and $Ma_{min} > 1.0$ indicated the separated scramjet mode. These two cases are representations of low-pressure and high-pressure cases in the first hysteresis loop shown in Fig. 6, respectively. Thus, the first hysteresis and relevant catastrophes occurred in the separated/shock-free scramjet mode transition region.

Fig. 9 shows typical 1- D p/p_{ref} and Ma distributions at target ER = 0.64 and ER = 0.68 conditions in historical ER-increasing path, respectively. Compared to ER = 0.42 case in Fig. 8, the current two cases had higher streamwise pressures because of higher ERs. Meanwhile, $Ma_{min} > 1.0$ indicated they were also in the separated scramjet mode. Other cases in the above Fig. 6 had ERs lower than 0.68, indicating lower wall-pressures, and thus no case was in the ramjet mode. Consequently, the second hysteresis and relevant catastrophes occurred in the separated scramjet mode, quite different from

Table 2 Catastrophe degrees of cavity bottom pressure $\chi_{\bar{p}_{cv}}$ and thrust $\chi_{\bar{F}_{ta}}$ at different target ER conditions.

Target ER	0.20	0.30	0.58	0.64
$\chi_{\bar{p}_{cv}}$ (%)	70	71	5	7
$\chi_{\bar{F}_{ta}}$ (%)	40	44	11	12

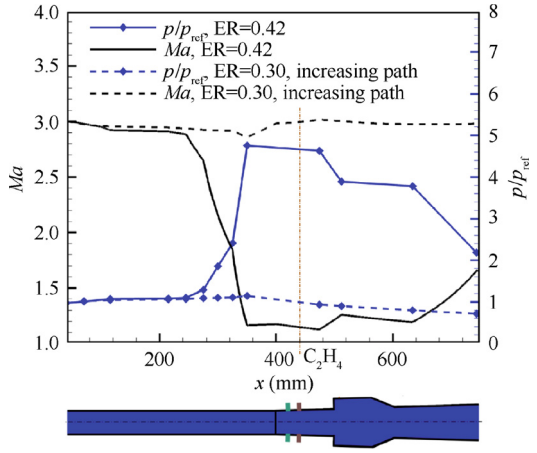

Fig. 8 Typical 1-D pressure p/p_{ref} and Mach number Ma distributions in the first hysteresis loop.

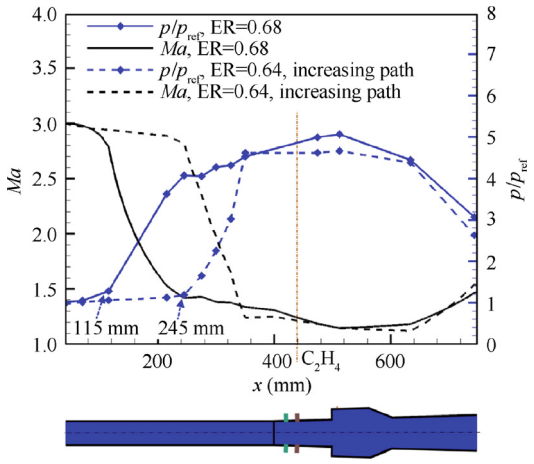

Fig. 9 Typical 1-D pressure p/p_{ref} and Mach number Ma distributions in the second hysteresis loop.

previous studies [2–5] of hysteresis and catastrophe in the ramjet/scramjet mode transition region. In other words, the current results indicate hysteresis and relevant catastrophes are not necessarily related to ramjet/scramjet mode transitions.

The two kinds of hysteresis and relevant catastrophes can also be preliminarily understood from the viewpoint of the intensive/weak combustion mode, which was not strictly defined by thrust performances. The cavity bottom pressure p_{cv} represent combustion pressure. Figs. 6 and 7 and Table 2 illustrate a higher combustion pressure resulted in a higher thrust performance. According to Brayton cycle analysis,[44,45] a higher combustion pressure indicates a higher thermal efficiency, and further indicates a higher thrust assuming constant heat release. On the other hand, high combustion pressure commonly generates flow separation, corresponding to the ramjet mode or the separated scramjet mode. Relatively, low combustion pressure does not generate flow separation, corresponding to the shock-free scramjet mode. Thus, the intensive/weak combustion modes could be more strictly defined as below. The intensive combustion mode is identified by a high thrust and combustion-zone pressures high enough to generate flow separation. The weak combustion mode is identified by a low thrust and low combustion-zone pressures generating no separation. Consequently, the first kind of hysteresis and relevant catastrophes occurred with transitions between the intensive combustion mode and the weak combustion mode, while the second kept in the intensive combustion mode.

3.2. Mechanism of the first hysteresis and obvious thrust catastrophes

The above Figs. 6 and 7 illustrate that the first hysteresis loop included two large catastrophes occurring in Cases A and B, respectively. ER was continuously regulated in Case A from initial ER = 0.30 condition to target ER = 0.42 condition using the historical ER-increasing path shown in Fig. 5. ER was continuously regulated in Case B from initial ER = 0.30 condition to target ER = 0.13 condition using the historical ER-decreasing path. As mentioned in Section 2.3, the flames at initial ER = 0.30 conditions were in the cavity shear-layer stabilized and jet-wake stabilized modes in Cases A and B, respectively. Hysteresis is strongly related to the relevant catastrophes. Thus, to clarify in-depth mechanism of the first hysteresis, this section analyzes catastrophes in Cases A and B in details, particularly from the view of flow and flame structural evolutions.

The catastrophe when ER regulated from initial ER = 0.30 to target ER = 0.42 in historical ER-increasing path is illustrated first. Fig. 10 is streamwise wall-pressure distribution time history of Case A. The pressures are normalized with the reference pressure p_{ref} given in Section 2.3. Fig. 11 is the corresponding thrust F_{ta} and ER time histories of Case A. The wall-pressure evolution could be divided into I, II, III and IV stages based on the variation feature of streamwise pressure-rises, particularly the pressure-rise origin. Stage I was in the shock-free scramjet mode, mostly at initial ER = 0.30 condition whose 1-D flow distribution is illustrated in the above Fig. 8. The streamwise pressures were low and close to the inflow pressure, and thus F_{ta} was relatively low as shown in Fig. 11. As ER increased, wall-pressures gradually increased downstream the cavities. Then as ER further increased, streamwise wall-pressures underwent abrupt increases in Stage II, especially near the cavities and injectors. The pressure-rise origin abruptly moved upstream to about $x = 300$ mm ahead of the injectors, and a higher pressure-rises of about 2.6 occurred near the injectors. This indicated the occurrence of combustion-induced shocks and large flow separation around the injectors. Meanwhile, transition from the shock-free scramjet mode to the separated scramjet mode happened according to 1-D analyses like Fig. 8. The abrupt increase of wall-pressure distribution in the expansive duct benefit thrust, and thus F_{ta} abruptly increased in Stage II as shown in Fig. 11. Then as ER kept increasing in Stage III, it remained in the separated scramjet mode. Meanwhile, the peak pressure-rise near the injectors gradually increased to about 4.6, indicating the strengthening of combustion-induced shocks. Soon after ER stopped increasing in Stage IV, streamwise wall-pressure distribution achieved the stabilized state at target ER = 0.42 condition. F_{ta} in this stage was obviously higher than Stage I as shown in Fig. 11.

Stages I and IV was the initial and final states in Fig. 10. Their typical 1-D flow distributions have been plotted in Fig. 8. To view their flame and flow structures, Fig. 12 displays the typical 2-D images of CH* chemiluminescence and simultaneous shadowgraph. For direct view of heat release intensity, CH* chemiluminescence images are transformed from original

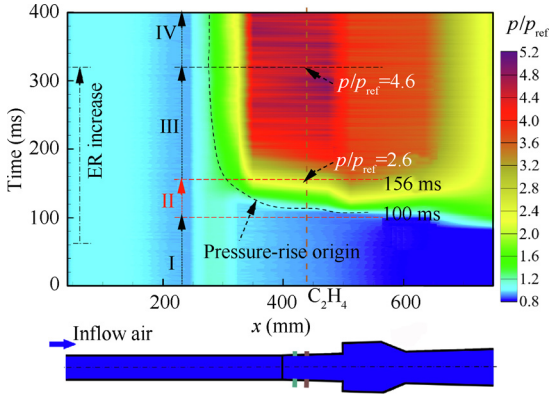

Fig. 10 Streamwise wall-pressure distribution time history of Case A.

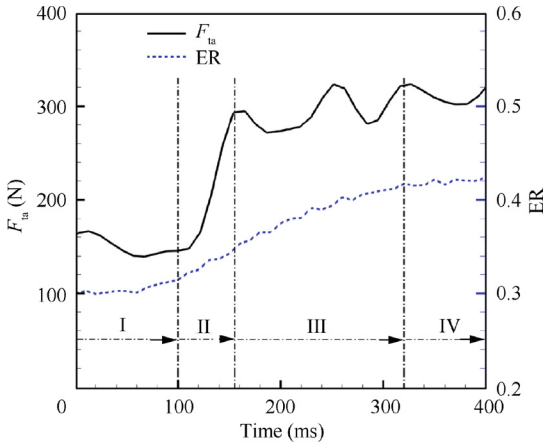

Fig. 11 Thrust F_{ta} and ER time histories of Case A.

grayscales to pseudo-colors. The color bars are normalized between 0–1 by the same luminescence intensity close to the highest. For clear view of shocks in shadowgraph images, green-dashed lines marked injection bow shocks by interactions of jet flow and supersonic main-flow, and yellow-dashed lines marked the pre-combustion shocks by downstream heat release induced pressure-rise. In Stage I, Fig. 12 (a) shows the flame was in the cavity shear-layer stabilized mode. No heat release occurred upstream the cavities or in the recirculation zones, and only weak heat release occurred near the cavity shear-layer and aft-wall. The low pressure-rises as shown in Figs. 8 and 10 generated no flow separation. Thus, only injection bow shocks existed, indicating the main flow was supersonic without separation. Differently, in Stage IV, the flame was in the jet-wake stabilized mode as shown in Fig. 12(b). The flame was strong, and widespread flame occurred upstream the cavities. The high pressure-rises as shown in Figs. 8 and 10, could generate flow separation. Thus, pre-combustion shocks occurred. Comparing the two shadowgraph images in Fig. 12, the irregular stripes near the injectors in Fig. 12(b) indicated heat release or flow separation, and the relatively regular pattern in Fig. 12(a) meant no heat release and separation.

To deeply understand the abrupt increase of wall-pressures in Stage II of Fig. 10, Figs. 13 and 14 display typical CH* chemiluminescence and shadowgraph images, respectively. Injection bow shocks are marked with green-dashed lines, and the most upstream combustion-induced shocks in view are marked with yellow-dashed lines. Figs. 13 and 14 illustrate abrupt change of flame and flow structures in Stage II. At first, as shown in Figs. 13(a), (b), the flame intensified near the cavity shear-layer and recirculation zone as ER further increased. But the injection bow shocks indicated no flow separation upstream the cavities, as shown in Figs. 14(a), (b). Stronger heat release could reduce flow speed while increasing temperature and pressure. These could increase residence time and shorten ignition delay time, and thus benefit flame propagation. Then as Fig. 13(c) displays, the flame developed much stronger and some flame occurred upstream the cavities. The stronger heat release caused higher pressure-rises, generating larger flow separation, and the relevant shock occurred upstream the cavities, as shown in Fig. 14(c). This shock-separation structure could further reduce flow speed, and promote combustion. Thus, as shown in Figs. 13(d)–(f), the flame became more and more stronger, and propagated further upstream and occurred ahead of the injectors. As the flame propagated, high pressure-rise region also occurred upstream the injectors, as shown in Fig. 10. Meanwhile, Figs. 14(d)–(f) display the shocks moved upstream, indicating flow separation near the injectors. Flow separation meant much higher combustion efficiency than no separation. Thus, the flame kept intensifying as ER kept increasing as shown in Figs. 13(g)–(h). Meanwhile, flow separation became stronger, showing as the shocks became further away from the injectors shown in Figs. 14(g)–(h). Across the above process, the flame transited from the cavity shear-layer stabilized mode to the jet-wake stabilized mode, and flow separation established upstream the cavities. The following flame and flow structural evolutions can be easily inferred from Fig. 10. In Stage III, the jet-wake stabilized flame further intensified as ER continuously increased, causing higher pressure-rises. Then in Stage IV,

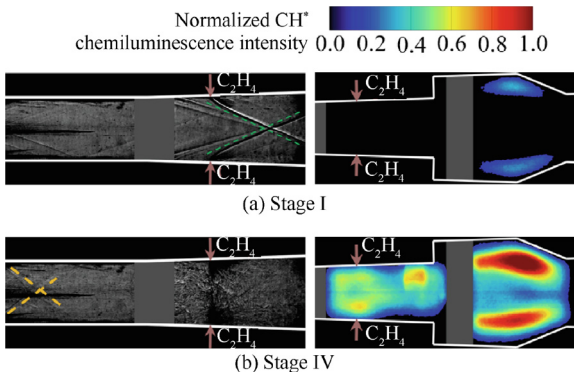

Fig. 12 Typical shadowgraph and CH* chemiluminescence images in Stages I and IV.

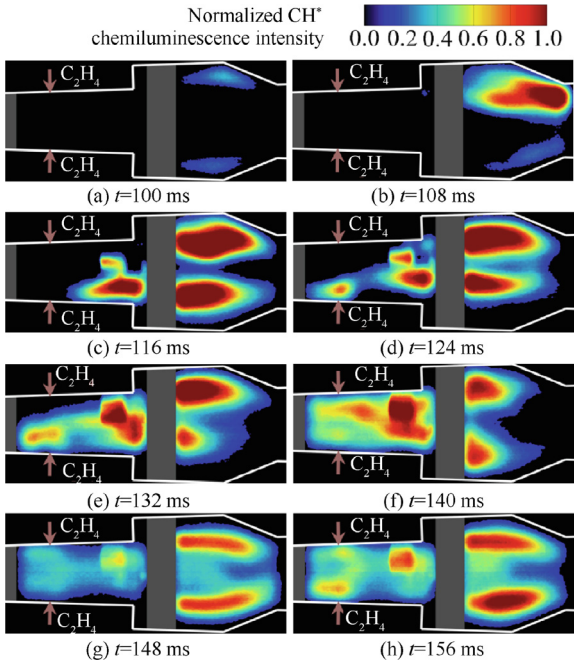

Fig. 13 Typical CH* chemiluminescence images in Stage II.

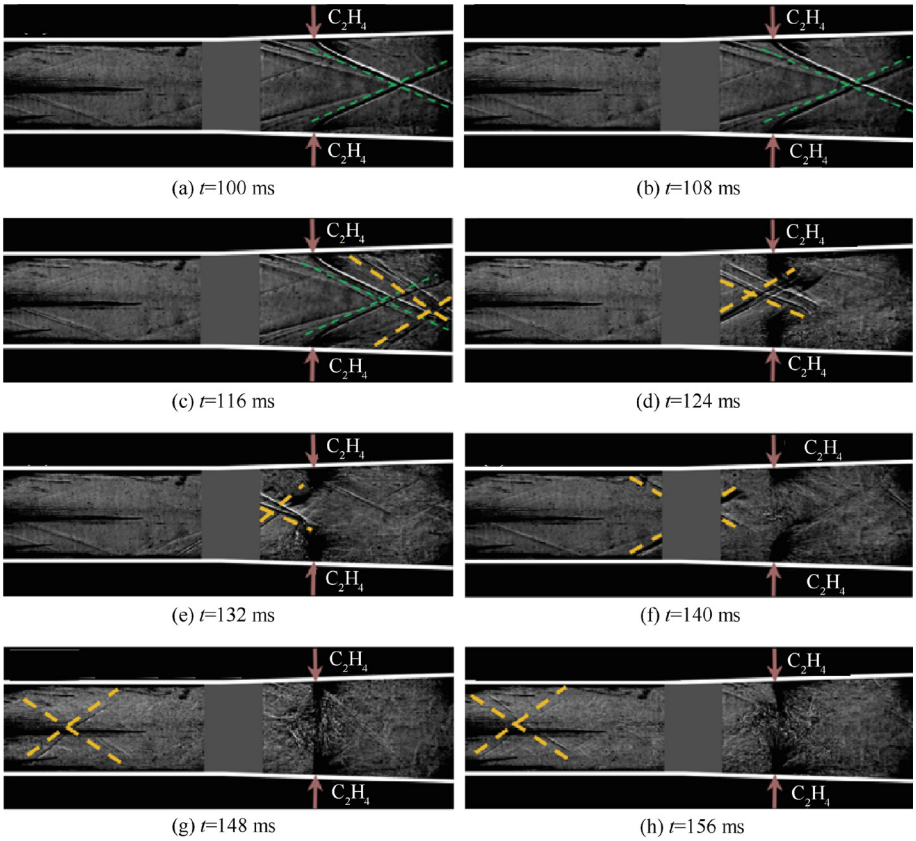

Fig. 14 Simultaneous shadowgraph images in Stage II.

soon after ER stopped increasing, interaction between the jet-wake stabilized flame and the separation induced shock-train achieved balance. Thus, the streamwise pressure distribution at target ER = 0.40 condition was achieved, as shown in Figs. 8 and 10. From the above, the catastrophe in historical ER-increasing path of the first hysteresis was attributed to flame stabilization mode transition from the cavity shear-layer stabilized to the jet-wake stabilized. Meanwhile, this transition caused establishment of flow separation and shocks upstream the cavities.

The catastrophe in historical ER-increasing path of the first hysteresis loop is illustrated above. The inverse catastrophe was observed in Case B when ER was regulated from initial ER = 0.30 to target ER = 0.13 in historical ER-decreasing path. This catastrophe is illustrated detailedly below. Fig. 15 displays the streamwise wall-pressure distribution time history. Fig. 16 is the corresponding thrust F_{ta} and ER time histories and could be divided into V, VI, VII and VIII stages as usual. The Stages V and VI were in the separated scramjet mode with 1-D flow distributions like the distribution at ER = 0.42 shown in Fig. 8. Continuous ER decrease in Stage VI caused gradual wall-pressure and decrease as shown in Figs. 15 and 16. The pressure-rise near the injectors gradually decreased from 3.2 to 1.6, and pressure-rise origin gradually moved downstream from about $x = 300$ mm to $x = 350$ mm. Then as ER further decreased, wall-pressure and F_{ta} catastrophes occurred in Stage VII. Streamwise wall-pressures abruptly decreased especially near the injectors and cavities, along with disappearance of the pressure-rise origin. The abrupt wall-pressure decreases in the expansive duct impaired thrust, and thus F_{ta} abruptly decreased. Meantime, transition from the separated scramjet mode to the shock-free scramjet mode happened by 1-D analyses like Fig. 8. Then in Stage VIII, the streamwise wall-pressure distribution varied little as ER decreased. After ER stopped decreasing, it kept in the shock-free scramjet mode at target ER = 0.13 condition, whose 1-D flow distribution was similar to the distribution at ER = 0.30 shown in Fig. 8. Compared to the wall-pressure and F_{ta} variations during the increase of ER in the above Figs. 10 and 11, the inverse variation features in this condition were similar. But the critical transition ER here was lower, resulting in relatively smaller wall-pressure and thrust catastrophes.

To deeply understand the catastrophe in Stage VII, Figs. 17 and 18 display the typical 2-D images of CH* chemiluminescence and simultaneous shadowgraph, respectively. At first as shown in Figs. 17(a)–(d), the flame weakened rapidly as ER further decreased, and even disappeared upstream the cavity. Meantime, the shocks moved downstream, but still existed upstream the cavities, as shown in Figs. 18(a)–(d). The shock movements here and the wall-pressure reductions in Fig. 15 together indicated recession of flow separation. This recession meant higher flow speed upstream the cavities, which in return suppressed combustion. Thus, as shown in Fig. 17(e), the flame further weakened, and only existed downstream the cavity fore-wall. Meantime, combustion-induced shocks disappear upstream the cavities as shown in Fig. 18(e), indicating not enough heat release to support flow separation upstream the cavities any more. Without the aid of flow separation, combustion efficiency would be much lower. Thus, the flame became

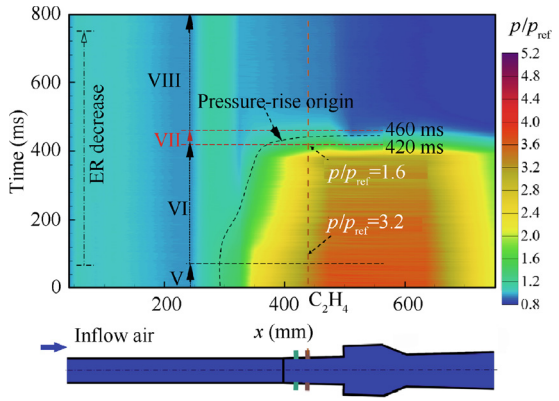

Fig. 15 Streamwise wall-pressure distribution time history of Case B.

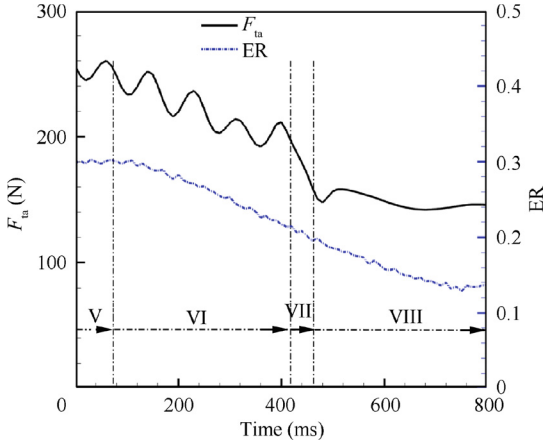

Fig. 16 Thrust F_{ta} and ER time histories of Case B.

quite weak, and could only stabilize near the low-speed cavity shear-layer as shown in Fig. 17(f). The injection bow-shocks in Fig. 18(f) indicated that the main flow was supersonic without separation upstream the cavities. From the above, the catastrophe in historical ER-decreasing path of the first hysteresis was attributed to flame stabilization mode transition from the jet-wake stabilized to the cavity shear-layer stabilized. Meanwhile, this transition caused vanishment of flow separation and shocks upstream the cavities.

In summary, wall-pressure and thrust catastrophes in the first hysteresis loop occurred because of the flame stabilization mode transitions between the jet-wake stabilized and the cavity shear-layer stabilized, along with the establishment and vanishment of shock/flow separation upstream the cavities, respectively. Across each transition, large changes in flame and shock/flow separation distributions resulted in large changes of wall-pressure distributions in the expansive duct, and manifested as an obvious thrust catastrophe. Thrust catastrophe was larger in historical ER-increasing path than in historical ER-decreasing path, and the reason was as below. In historical ER-increasing path, the initial cavity shear-layer mode had low combustion efficiency because of no flow separation. ER should exceed a high critical value to generate enough heat release to trigger flow separation, and then the flame transited to the jet-wake stabilized. But in historical ER-decreasing path, the initial jet-wake stabilized mode had high combustion

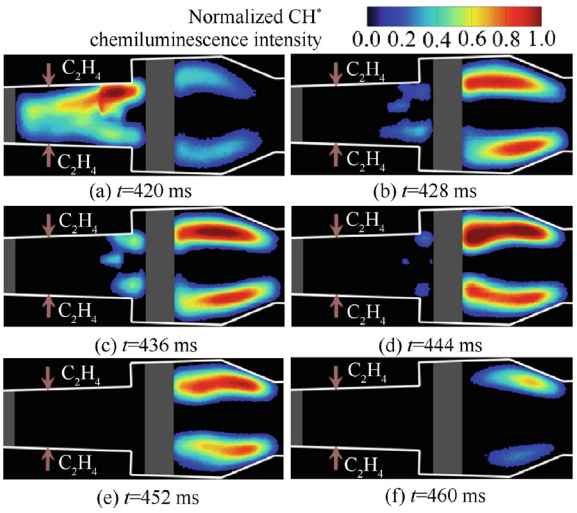

Fig. 17 Typical CH* chemiluminescence images in Stage VII.

efficiency because of flow separation. ER should reduce below a lower critical value to generate heat release not enough to maintain flow separation, and then the inverse transition to the cavity shear-layer stabilized occurred. The higher critical ER in historical ER-increasing path meant the larger thrust catastrophe, and difference between the two critical transition ERs resulted in the first hysteresis loop.

3.3. Mechanism of the second hysteresis and unobvious thrust catastrophes

The above Figs. 6 and 7 illustrate that the second hysteresis loop involved two small catastrophes occurring in Cases C and D, respectively. ER was continuously regulated in Case C from initial ER = 0.58 to target ER = 0.52 using the historical ER-decreasing path in Fig. 5. ER was continuously regulated in Case D from initial ER = 0.64 to target ER = 0.68 using the historical ER-increasing path. This section analyzes the catastrophes in Cases C and D in detail for in-depth clarification of the second hysteresis, particularly from the view of flow and flame structural evolutions.

The catastrophe when ER regulated from initial ER = 0.58 to target ER = 0.52 in historical ER-decreasing path is illustrated first. Fig. 19 is streamwise wall-pressure distribution time history of Case C. Fig. 20 is the corresponding thrust F_{ta} and ER time histories. The wall-pressure evolution could be divided into S1, S2, S3 and S4 stages as usual. Stage S1 was in the separated scramjet mode at initial ER = 0.58 condition with a similar 1-D flow distribution at ER = 0.68 shown in Fig. 9. The pressure-rise origin was at about $x = 115$ mm. Then in Stage S2, the cavity bottom pressure-rise decreased from 4.7 to 4.4, indicating heat release reduction because of ER decrease. But the pressure-rise origin changed little. The little decrease of wall-pressures in the expansive duct resulted in little change of F_{ta} as shown in Fig. 20. Then wall-pressure catastrophe happened in Stage S3, during which the pressure-rise origin abruptly moved downstream from $x = 115$ mm to $x = 245$ mm as shown in Fig. 19. The cavity bottom pressure-rise decreased from 4.4 to 4.1, along with slight wall-pressure decreases in the expansive duct, resulting

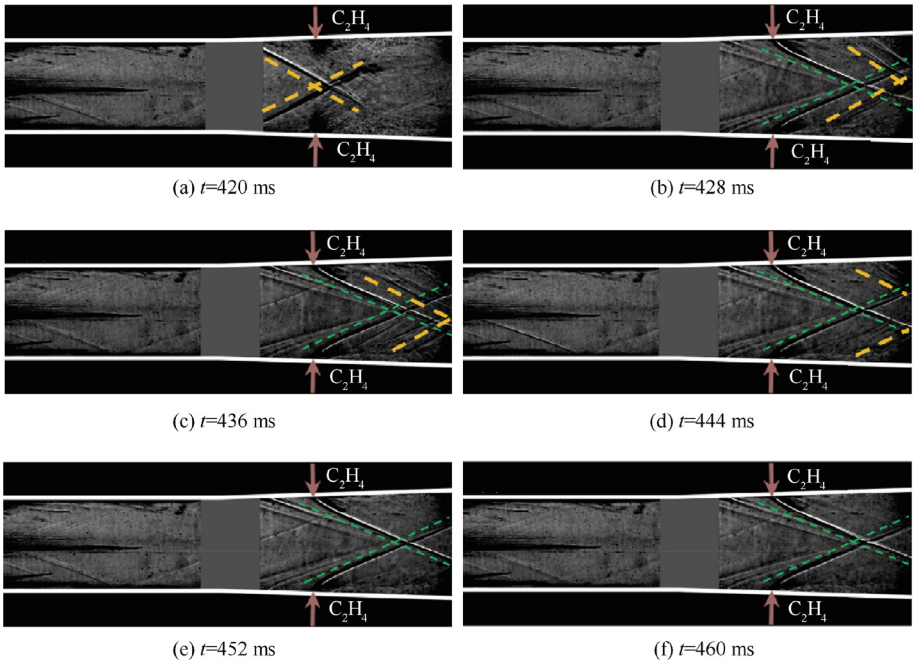

Fig. 18 Simultaneous shadowgraph images in Stage VII.

in slight decrease of F_{ta} as shown in Fig. 20. The enlarged F_{ta} decreasing rate indicated the thrust catastrophe. Then in Stage S4, as soon as ER stopped decreasing, streamwise wall-pressure distribution achieved the stabilized state at target ER = 0.52 condition as shown in Fig. 19. The 1-D flow distribution was similar to the distribution at ER = 0.64 shown in Fig. 9, but wall-pressures were slightly lower because the current ER of 0.52 was lower than 0.64. This stage still kept in the separated scramjet mode, and F_{ta} was slightly lower than Stage S1 as shown in Fig. 20.

Flame and flow evolutions from Stage S1 to Stage S4 can be preliminarily inferred from Fig. 19, including shock and flow separation intensities inferred from the pressure-rise origin. In Stage S1, the flame and flow structures were similar to the state at ER = 0.42 in Fig. 12(b). But current flame was stronger with stronger shocks and larger separation because current ER of 0.58 was higher than 0.42. In Stage S2, heat release gradually decreased as ER decreased, showing as gradual decreases of combustion-zone pressure-rises near the cavities. But the almost constant pressure-rise origin indicated the shocks and flow separation changed little. In Stage S3, combustion-zone pressure-rises decreased to levels not enough to sustain the shock/flow separation structures. Balance between flame and shocks was broken, and resulted in the catastrophe. The obvious downstream movement of pressure-rise origin in Fig. 19 indicated flow separation changed obviously smaller. In Stage S4, the smaller separation could achieve balance with the slightly lower combustion-induced pressure-rises.

To better understand the wall-pressure catastrophe in Stage S3, this stage is divided into four equal time intervals. Fig. 21 displays the time-averaged distributions and standard deviations of CH* chemiluminescence in these time intervals, which mean the time-averaged distributions and instabilities of heat release, respectively. Fig. 22 displays typical shadowgraph

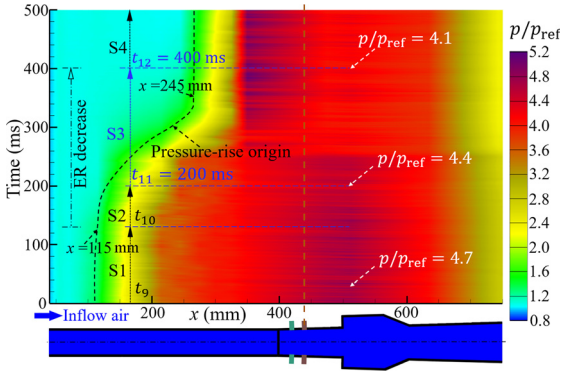

Fig. 19 Streamwise wall-pressure distribution time history of Case C.

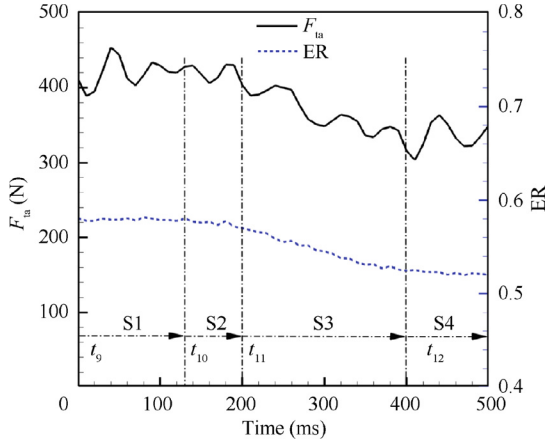

Fig. 20 Thrust F_{ta} and ER time histories of Case C.

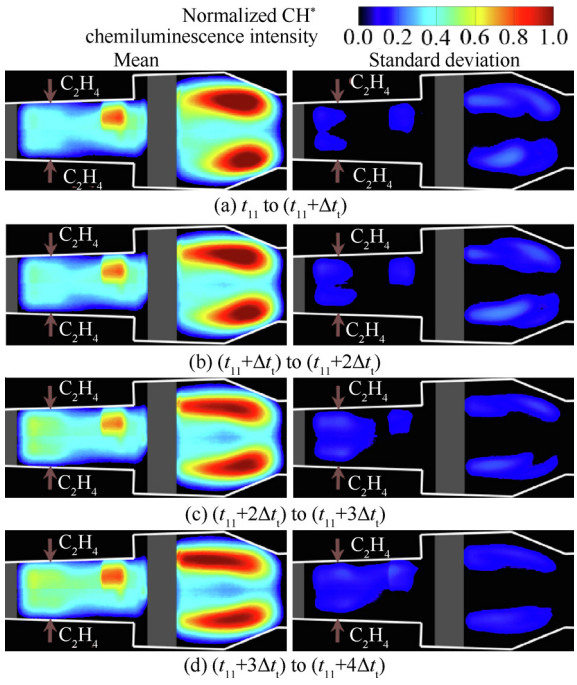

Fig. 21 Means and standard deviations of CH* chemiluminescence images in Stage S3 ($\Delta t_t = 50$ ms).

images in this stage. Fig. 21 illustrates the flame kept in the jet-wake stabilized mode across the catastrophe. The time-averaged shape of core flame region changed from elliptical to slender near the cavities, indicating the flame slightly weakened. Thus, it manifested as the slight decrease of pressure-rise near the cavities in Fig. 19. Fig. 21 also illustrates the flame instability changed a little as shown in the standard deviation images. The smaller oscillating region and lower amplitudes near the cavities indicated local flame became more stabilized, while the flame was less stabilized upstream the cavities. Meanwhile, as the flame weakened, Fig. 22 illustrates the shocks also changed a little. The shocks in view moved obviously closer to the injectors, together with the downstream movement of the pressure-rise origin in Fig. 19, indicating smaller flow separation. This also agreed with former numerical study,[41] in which the pressure-rise origin movement originated from less shock reflections, namely a shorter shock-train. The smaller flow separation meant smaller low-speed region, which was adverse for combustion. Then after ER stopped decreasing, the smaller flow separation could match the weakened flame, which remained in the jet-wake stabilized mode at target ER = 0.52 condition.

As illustrated above, there are two slightly different flame/flow structural states across the catastrophe from Stage S2 to S4. The former state S2 had slightly stronger flame with slightly larger flow separation and longer shock-train. They were manifested as higher combustion-zone pressure-rises near the cavities, and the pressure-rise origin closer to the inlet. The latter state S4 behaved inversely. Thus, the main difference of these two states is the coupling interaction between the flame and the shock/flow structures in the jet-wake stabilized mode. For easy description, the former state is named as the flame/shock intensive interaction mode, and the latter is named as

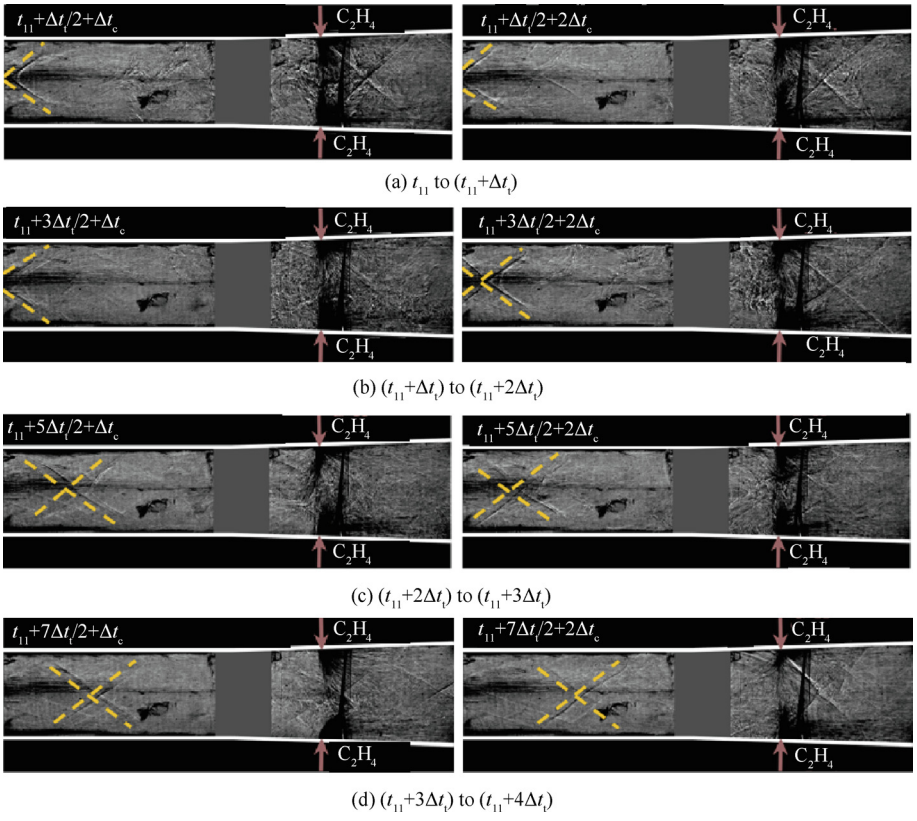

Fig. 22 Typical shadowgraph images in Stage S3 ($\Delta t_t = 50$ ms, $\Delta t_c =$ 0.5 ms).

the flame/shock weak interaction mode. In other words, the catastrophe in historical ER-decreasing path of the second hysteresis was attributed to flame/shock interaction mode transition from the intensive interaction mode to the weak interaction mode. Across the transition, the flame became slightly weaker with smaller flow separation, showing slightly lower pressure-rises near the cavities and obviously downstream movement of the pressure-rise origin.

The catastrophe in historical ER-decreasing path of the second hysteresis loop is illustrated above. The inverse catastrophe in Case D with ER from initial ER = 0.64 to target ER = 0.68 in historical ER-increasing path is illustrated as below. Fig. 23 displays the streamwise wall-pressure distribution time history. Fig. 24 is the corresponding thrust F_{ta} and ER time histories. The wall-pressure evolution could be divided into S5, S6, S7 and S8 four stages as usual. Stage S5 was in the separated scramjet mode at initial ER = 0.64 condition with the 1-D flow distribution illustrated in the above Fig. 9. The pressure-rise origin was at about $x = 245$ mm. Then a little while as ER increased in Stage S6, catastrophe occurred as the pressure-rise origin abruptly moved upstream from $x = 245$ mm to $x = 115$ mm. Meantime, wall-pressures slightly increased in the expansive duct as the cavity bottom pressure-rise increased from 4.7 to 5.0. This resulted in a slight F_{ta} increase as shown in Fig. 24. The enlarged F_{ta} increasing rate indicated the thrust catastrophe. In Stage S7, though ER still continuously increased, the streamwise wall-pressures changed little, resulting in little change of F_{ta}. In Stage S8, as ER stopped increasing, the streamwise wall-pressure distribution achieved the stabilized state at target ER = 0.68 condition with the 1-D flow distribution shown in the above Fig. 9. This stage still kept in the separated scramjet mode, and F_{ta} was slightly higher than in Stage S5 as shown in Fig. 24. Compared to the wall-pressure and F_{ta} variations during ER decreasing in the above Figs. 19 and 20, the inverse variation features here during ER increasing were similar. The pressure-rise origins across the catastrophes were almost the same. Though the critical transition ER here was slightly higher, thrust catastrophe here was similarly small as obvious wall-pressure variations only occurred in the constant-area duct.

To directly understand the small catastrophe in Stage S6, this stage is divided into two equal time intervals. Fig. 25 displays the time-averaged distributions and standard deviations

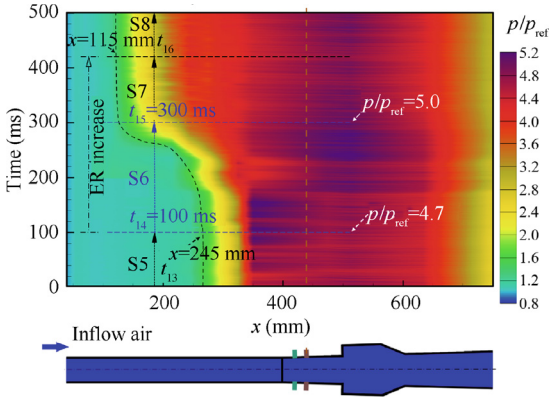

Fig. 23 Streamwise wall-pressure distribution time history of Case D.

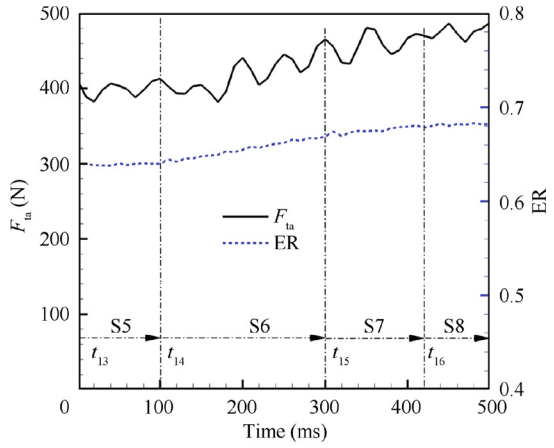

Fig. 24 Thrust F_{ta} and ER time histories of Case D.

of CH* chemiluminescence images. Fig. 26 displays typical shadowgraph images. Fig. 25 illustrates the flame kept in the jet-wake stabilized mode across the catastrophe. The time-averaged shape of core flame region changed from slender to elliptical near the cavities, indicating the flame slightly intensified. The flame instability also changed a little as shown in the standard deviation images. The larger oscillating region and higher amplitudes near the cavities indicated that local flame became less stabilized, while it was more stabilized near the injectors. Meanwhile as flame intensified, Fig. 26 illustrates the shocks also changed a little. The shocks in view farther away from the injectors here and the upstream movement of the pressure-rise origin in Fig. 23 indicated larger flow separation. This also agreed with former numerical study,[41] in which the movement of the pressure-rise origin originated from more shock reflections, namely a longer shock-train. The larger flow separation meant larger low-speed region, which was beneficial for combustion. Then after ER stopped increasing, the larger flow separation could match the intensified flame, which kept in the jet-wake stabilized mode at target ER = 0.68 condition. Above all, the catastrophe in historical ER-increasing path of the second hysteresis can also be described from the view of interactions between flame and shock/flow structures. It was attributed to flame/shock interaction mode transition from the weak interaction mode to the intensive interaction mode. The flame became slightly stronger with larger flow separation,

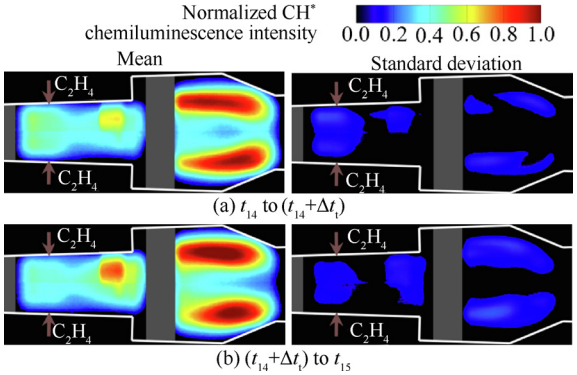

Fig. 25 Means and standard deviations of CH* chemiluminescence images in Stage S6 ($\Delta t_t = 100$ ms).

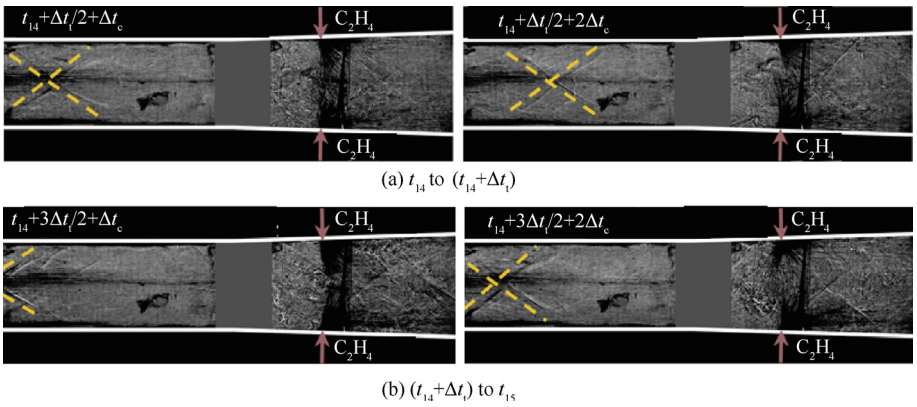

(a) t_{14} to $(t_{14}+\Delta t_t)$

(b) $(t_{14}+\Delta t_t)$ to t_{15}

Fig. 26 Typical shadowgraph images in Stage S6 ($\Delta t_t = 100$ ms, $\Delta t_c = 0.5$ ms).

showing as slightly higher pressure-rises near the cavities and obviously upstream movement of the pressure-rise origin.

In summary, catastrophes in the second hysteresis loop occurred in the jet-wake stabilized mode because of the flame/shock interaction mode transitions between the weak interaction mode and the intensive interaction mode. Across each transition, the flame became slightly stronger/weaker with larger/smaller flow separation. Meantime, pressure-rises near the cavities became slightly higher/lower, and the pressure-rise origin obviously moved upstream/downstream. Small changes in flame and shock/flow separations resulted in small changes of wall-pressure distributions in the expansive duct, while the obvious change of separation in the constant-area isolator had no effect on thrust. Thus, thrust catastrophe was unobvious. In historical ER-increasing path, the initial flame/shock weak interaction mode had smaller flow separation, indicating slightly lower combustion efficiency. ER should exceed a slightly higher critical value to generate enough heat release for higher combustion-zone pressure-rises to induce the change of shock/flow separation structure. Then, it transited to the flame/shock intensive interaction mode. But in historical ER-decreasing path, the initial intensive interaction mode had larger flow separation, indicating slightly higher combustion efficiency. ER should reduce below a slightly lower critical value to generate heat release not enough to maintain the current shock/flow separation structure, and then the inverse transition occurred. The difference between the two critical transition ERs resulted in the second hysteresis loop.

4. Conclusions

This paper studied hysteresis and catastrophe phenomena during continuous ER regulations in a cavity-based ethylene-fueled scramjet combustor by direct-connect combustion tests. The combustor consisted of a constant-area isolator and an expansive duct. The popular combination of cavity flameholders and upstream fuel injection were used in the expansive duct. The inflow Mach number, stagnation temperature and stagnation pressure were 3.0, 1657 K and 2100 kPa, respectively. Fuel ER was continuously regulated by a multi-step manner to explore the influence of historical ER variation directions. Combustion flow data including wall-pressures, thrusts and high-speed images of shadowgraphs and CH* chemiluminescence were obtained. Results display two divided hysteresis loops. Each had two relevant catastrophes of wall-pressures and thrusts. Occurrence mechanisms of the hystereses and catastrophes are elucidated from the viewpoint of flame and shock/flow separation structures. Main conclusions are as follows:

(1) This work observed a two-loop hysteresis phenomenon signifying two kinds of combustion hysteresis, while previous experimental studies [2–5,26] only observed one-loop. From the view of 1-D flow estimations of thermal choking, the first kind of hysteresis and relevant catastrophes occurred in the shock-free/separated scramjet mode transition region, but the second kept in the separated scramjet mode. This broke through the traditional knowledge that hysteresis and catastrophe were surely related to transitions between the ramjet mode and the scramjet mode.

(2) The first hysteresis and relevant catastrophes were attributed to flame stabilization mode transitions between the cavity shear-layer stabilized and the jet-wake stabilized, accompanied by flow separation establishment/vanishment upstream the cavities. Through each transition, large changes of flame and shock/flow separation structures generated large changes of wall-pressure distributions in the expansive duct, and manifested as an obvious thrust catastrophe. Besides, thrust catastrophe was larger in historical ER-increasing path than ER-decreasing. This was because combustion efficiency was low in the cavity shear-layer stabilized mode owing to no flow separation upstream the cavities. Then, a higher critical ER signifying a larger catastrophe was required to generate enough heat release to trigger flow separation and induce the transition in historical ER-increasing path. Difference between the two critical transition ERs resulted in the first hysteresis.

(3) The second hysteresis and relevant catastrophes occurred in the jet-wake stabilized mode. They were attributed to the flame/shock interaction mode transitions between the flame/shock weak interaction mode and the flame/shock intensive interaction mode. Each transition resulted in slightly stronger/weaker flame along with larger/smaller flow separation, and showed as slightly higher/lower pressure-rises near the cavities and obviously upstream/downstream movement of the pressure-rise origin. This meant small changes of wall-pressure distributions in the expansive duct, along with obvious changes in the constant-area isolator which did not benefit thrust, and

thus thrust catastrophe was unobvious. Hysteresis occurred as the critical transition ER was slightly higher in ER-increasing path because the initial flame/shock weak interaction mode had slightly lower combustion efficiency owing to smaller flow separation. Then, ER should exceed a slightly larger critical value to generate enough heat release to induce the change of shock/flow separation structure, and trigger the transition.

Declaration of Competing Interest

The authors declare that they have no known competing financial interests or personal relationships that could have appeared to influence the work reported in this paper.

Acknowledgements

This work was supported by the National Natural Science Foundation of China (Nos. 11902325 and 11672309).

References

1. Heiser W, Pratt D, Daley D, et al. *Hypersonic airbreathing propulsion*. Reston: AIAA; 1994.
2. Rockwell RD, Goyne CP, Haw W, Krauss RH, McDaniel JC, Trefny CJ. Experimental study of test-medium vitiation effects on dual-mode scramjet performance. *J Propuls Power* 2011;**27**(5):1135–42.
3. Wei BX, Zhang Y, Tian L, et al. Experimental study on combustion mode transition in an aero-ramp based scramjet. Reston: AIAA; 2012, Report No.: AIAA-2012-3923.
4. Bao W, Yang Q, Chang J, Zong Y, Hu J. Dynamic characteristics of combustion mode transitions in a strut-based scramjet combustor model. *J Propuls Power* 2013;**29**(5):1244–8.
5. Zhu SH, Xu X. Experimental study on mode transition of the dual-mode scramjet with two-staged-strut injectors. *Proc Inst Mech Eng Part G: J Aerosp Eng* 2018;**232**(10):1864–74.
6. Arnol'd VI. *Bifurcation theory and catastrophe theory*. Heidelberg, Berlin: Springer; 1999.
7. Zhang C, Chang J, Feng S, Ma J, Zhang J, Bao W. Pressure rising slope variation accompanying with combustion mode transition in a dual-mode combustor. *Aerosp Sci Technol* 2017;**68**:370–9.
8. Xiao BG, Li L, Zhang SP, et al. Direct-connect experimental investigation of combustion mode transition for scramjet engine. *J. Propuls Tech* 2019;**40**(2):340–5 [Chinese].
9. Mitani T, Hiraiwa T, Sato S, Tomioka S, Kanda T, Tani K. Comparison of scramjet engine performance in Mach 6 vitiated and storage-heated air. *J Propuls Power* 1997;**13**(5):635–42.
10. Ueda S, Tomioka S, Ono F, et al. *Mach 6 test of a scramjet engine with multi-staged fuel injection*. Reston: AIAA; 2006, Report No.: AIAA-2006-1027.
11. Kouchi T, Masuya G, Mitani T, Tomioka S. Mechanism and control of combustion-mode transition in a scramjet engine. *J Propuls Power* 2012;**28**(1):106–12.
12. Turner JC, Smart MK. Mode change characteristics of a three-dimensional scramjet at Mach 8. *J Propuls Power* 2013;**29**(4):982–90.
13. Yu DR, Cui T, Bao W. Catastrophe, hysteresis and bifurcation of mode transition in scramjet engines and its model. *Sci China Ser E: Technol Sci* 2009;**52**(6):1543–50.
14. Wang ZP, Gu HB, Cheng LW, Zhong FQ, Zhang XY. CH* luminance distribution application and a one-dimensional model of the supersonic combustor heat release quantization. *Int J Turbo Jet Engines* 2019;**36**(1):45–50.
15. Yang Q, Bao W, Chetehouna K, Zhang S, Gascoin N. Thermal behavior of an isolator with mode transition inducing back-pressure of a dual-mode scramjet. *Chin J Aeronaut* 2017;**30**(2):595–601.
16. Tian Lu, Chen L, Chen Q, Li F, Chang X. Quasi-one-dimensional multimodes analysis for dual-mode scramjet. *J Propuls Power* 2014;**30**(6):1559–67.
17. Cao R, Lu Y, Yu D, Chang J. Study on influencing factors of combustion mode transition boundary for a scramjet engine based on one-dimensional model. *Aerosp Sci Technol* 2020;**96**:105590.
18. Fotia ML, Driscoll JF. Isolator-combustor interactions in a direct-connect ramjet-scramjet experiment. *J Propuls Power* 2012;**28**(1):83–95.
19. Fotia ML, Driscoll JF. Ram-scram transition and flame/shock-train interactions in a model scramjet experiment. *J Propuls Power* 2012;**29**(1):261–73.
20. Chen B, Xu Xu, Wei B, Zhang Y. Numerical simulations of turbulent flows in aeroramp injector/gas-pilot flame scramjet. *Chin J Aeronaut* 2017;**30**(4):1373–90.
21. Zhang Y, Chen B, Liu G, et al. Influencing factors on the mode transition in a dual-mode scramjet. *Acta Astronaut* 2014;**103**:1–15.
22. Zhang J, Chang J, Wang Zi'ao, Gao L, Bao W. Flame propagation and flashback characteristics in a kerosene fueled supersonic combustor equipped with strut/wall combined fuel injectors. *Aerosp Sci Technol* 2019;**93**:105303.
23. Chang J, Zhang J, Bao W, Yu D. Research progress on strut-equipped supersonic combustors for scramjet application. *Prog Aerosp Sci* 2018;**103**:1–30.
24. Deng W, Le J, Yang S, Zhang W, Tian Ye. Experimental research of air-throttling ignition for a scramjet at Ma 6.5. *Chin J Aeronaut* 2017;**30**(3):932–8.
25. Li F, Sun M, Zhu J, et al. Scaling effects on combustion modes in a single-side expansion kerosene-fueled scramjet combustor. *Chin J Aeronaut* 2021;**34**(5):684–90.
26. Feng S, Chang J, Zhang C, Wang Y, Ma J, Bao W. Experimental and numerical investigation on hysteresis characteristics and formation mechanism for a variable geometry dual-mode combustor. *Aerosp Sci Technol* 2017;**67**:96–104.
27. Yang QC, Chang JT, Bao W, et al. A mechanism of combustion mode transition for hydrogen fueled scramjet. *Int J Hydrog Energy* 2014;**39**(18):9791–7.
28. Sullins GA. Demonstration of mode transition in a scramjet combustor. *J Propuls Power* 1993;**9**(4):515–20.
29. Micka DJ, Driscoll JF. Combustion characteristics of a dual-mode scramjet combustor with cavity flameholder. *Proc Combust Inst* 2009;**32**(2):2397–404.
30. Micka DJ. Combustion stabilization, structure, and spreading in a laboratory dual-mode scramjet combustor [dissertation]. Ann Arbor: University of Michigan; 2010.
31. Yuan Y, Zhang T, Yao W, Fan X. Study on flame stabilization in a dual-mode combustor using optical measurements. *J Propuls Power* 2015;**31**(6):1524–31.
32. Yuan Y, Zhang T, Yao W, Fan X, Zhang P. Characterization of flame stabilization modes in an ethylene-fueled supersonic combustor using time-resolved CH* chemiluminescence. *Proc Combust Inst* 2017;**36**(2):2919–25.
33. Nakaya S, Kinoshita R, Lee J, Ishikawa H, Tsue M. Analysis of supersonic combustion characteristics of ethylene/methane fuel mixture on high-speed measurements of CH* chemiluminescence. *Proc Combust Inst* 2019;**37**(3):3749–56.
34. Tian Ye, Zeng X, Yang S, Xiao B, Zhong F, Le J. Experimental study on flame development and stabilization in a kerosene fueled supersonic combustor. *Aerosp Sci Technol* 2019;**84**:510–9.
35. Wang H, Song X, Li L, Huang Y, Sun M. Lean blowoff behavior of cavity-stabilized flames in a supersonic combustor. *Aerosp Sci Technol* 2021;**109**:106427.

36. Cai Z, Zhu J, Sun M, Wang Z. Effect of cavity fueling schemes on the laser-induced plasma ignition process in a scramjet combustor. *Aerosp Sci Technol* 2018;**78**:197–204.
37. Wang H, Wang Z, Sun M, Wu H. Combustion modes of hydrogen jet combustion in a cavity-based supersonic combustor. *Int J Hydrog Energy* 2013;**38**(27):12078–89.
38. Nakaya S, Hikichi Y, Nakazawa Y, et al. Ignition and supersonic combustion behavior of liquid ethanol in a scramjet model combustor with cavity flame holder. *Proc Combust Inst* 2015;**35**(2):2091–9.
39. Liu C, Sun M, Wang H, Yang L, An B, Pan Yu. Ignition and flame stabilization characteristics in an ethylene-fueled scramjet combustor. *Aerosp Sci Technol* 2020;**106**:106186.
40. Xiong P, Zheng D, Tan Yu, Tian Ye, Le J. Experimental study of ignition and combustion characteristics of ethylene in cavity-based supersonic combustor at low stagnation temperature and pressure. *Aerosp Sci Technol* 2021;**109**:106414.
41. Zhang Xu, Yue L, Huang T, Zhang Q, Zhang X. Numerical investigation of mode transition and hysteresis in a cavity-based dual-mode scramjet combustor. *Aerosp Sci Technol* 2019;**94**:105420.
42. Han Y, He Y, Tian Ye, Zhong F, Le J. Assessment of a hybrid RANS/LES simulation method and URANS method in depicting the unsteady motions of flow structures in a scramjet combustor. *Aerosp Sci Technol* 2018;**72**:114–22.
43. Huang W. Investigation on the effect of strut configurations and locations on the combustion performance of a typical scramjet combustor. *J Mech Sci Technol* 2015;**29**(12):5485–96.
44. Builder C. On the thermodynamic spectrum of airbreathing propulsion. Reston: AIAA; 1964. Report No.: AIAA-1964-0243.
45. Rutledge JL, Polanka MD. Efficiency of an ideal Brayton cycle with a constant-volume interturbine burner. *J Propuls Power* 2015;**31**(3):970–6.